Resonant tunneling across a ferroelectric domain wall

M. Li,[1] L. L. Tao,[1,*] J. P. Velev,[1,2] and E. Y. Tsymbal[1,†]

[1]*Department of Physics and Astronomy and Nebraska Center for Materials and Nanoscience, University of Nebraska, Lincoln, Nebraska 68588, USA*

[2]*Department of Physics and Astronomy, University of Puerto Rico, San Juan, Puerto Rico 00931, USA*

(Received 26 January 2018; published 10 April 2018)

Motivated by recent experimental observations, we explore electron transport properties of a ferroelectric tunnel junction (FTJ) with an embedded head-to-head ferroelectric domain wall, using first-principles density-functional theory calculations. We consider a FTJ with $La_{0.5}Sr_{0.5}MnO_3$ electrodes separated by a $BaTiO_3$ barrier layer and show that an in-plane charged domain wall in the ferroelectric $BaTiO_3$ can be induced by polar interfaces. The resulting V-shaped electrostatic potential profile across the $BaTiO_3$ layer creates a quantum well and leads to the formation of a two-dimensional electron gas, which stabilizes the domain wall. The confined electronic states in the barrier are responsible for resonant tunneling as is evident from our quantum-transport calculations. We find that the resonant tunneling is an orbital selective process, which leads to sharp spikes in the momentum- and energy-resolved transmission spectra. Our results indicate that domain walls embedded in FTJs can be used to control the electron transport.

DOI: 10.1103/PhysRevB.97.155121

I. INTRODUCTION

Ferroelectric materials are characterized by a spontaneous electric polarization, which can be reversed by an applied electric field [1]. This property is sustained down to the nanoscale dimensions [2–4], which makes ferroelectrics attractive for modern technological applications, such as nonvolatile random access memories and field sensors [5]. Nanoscale ferroelectrics found an important application in ferroelectric tunnel junctions (FTJs) [6–8]. A FTJ consists of two metal or semiconductor electrodes separated by a nanometer-thick ferroelectric barrier layer. The tunneling resistance of a FTJ is modulated by electric field induced ferroelectric polarization switching—the effect known as tunneling electroresistance (TER). Following the theoretical predictions [9,10], there have been a number of successful experimental demonstrations of the TER effect in trilayer junctions [11–16], showing the potential of FTJs for nonvolatile memory applications [17,18]. The structural and/or electronic asymmetry of the FTJ plays a decisive role for the TER effect. It can be achieved using dissimilar electrodes [9,19–22], through interface engineering [13,23–26], or applied bias [27,28]. Additionally, using ferromagnetic electrodes in a FTJ adds functionality, forming a multiferroic tunnel junction (MFTJ) [29]. Such a MFTJ constitutes a four-state resistance device where the tunneling resistance depends both on the relative magnetization of the electrodes and the polarization orientation of the ferroelectric barrier [30–34].

In parallel with this endeavor, there has been significant effort in exploring properties of ferroelectric domain walls—regions, which separate uniformly polarized domains in ferroelectric materials [35]. Normally, the domain walls carry no net bound charge, i.e. the normal component of the spontaneous polarization is continuous across the domain wall. Such a neutral domain wall is energetically favorable over a charged domain wall, where a bound charge appears at the wall due to discontinuity of the normal component of the polarization. In proper ferroelectrics, the occurrence of charged domain walls is often associated with availability of free carriers to compensate the polarization charge [36]. This leads to the electrical conductivity of the domain walls as has recently been reported for a number of different ferroelectric materials [37–45]. This property of ferroelectric domain walls can be exploited for developing a new type of nanoscale electronics [37,46].

To date, most of the work on electron transport properties of the domain walls has been focused on the electric current along the wall. Exploring the electron transport across the domain wall is much more challenging due to the insulating nature of the surrounding ferroelectric material. Very recently, Sanchez-Santolino *et al.* [47] were able to fabricate a MFTJ with ferromagnetic $La_{1-x}Sr_xMnO_3$ (LSMO) electrodes and a ferroelectric $BaTiO_3$ (BTO) tunnel barrier, where ferroelectric polarization of the BTO formed a head-to-head domain wall. Such a charged domain wall within the nanometer-thick barrier layer was stabilized by a confined electron gas formed at the domain wall. Due to the discrete electronic states resulting from the electric gas, signatures of resonant tunneling were observed, giving rise to quantum oscillations of the tunneling conductance. On the theoretical side, it has been shown that a head-to-head domain-wall structure can be created in a ferroelectric $PbTiO_3$ layer through the artificial electron doping at the interface [48], and such a domain wall can lead to spin-dependent resonant tunneling in a MFTJ [49]. These results demonstrate that a ferroelectric domain wall can be used as the controlling element of the transport properties of a FTJ [50].

Stimulated by these findings, in this work we explore electron transport properties of LSMO/BTO/LSMO tunnel

*ltao2@unl.edu
†tsymbal@unl.edu

junctions focusing on the effects of resonant tunneling across a ferroelectric domain wall. Using first-principles density-functional theory calculations, we show that a head-to-head domain wall can be stabilized within the BTO thin ferroelectric layer due to the polar LSMO/BTO interfaces and a two-dimensional electron gas (2DEG) confined at the domain wall. We find that electron transmission across the domain-wall FTJ exhibits clear signatures of resonant tunneling. We analyze the microscopic origin of the resonant tunneling mechanism using the calculated energy-dependent transmission, the transmission spectrum in the momentum space, the orbital-resolved local density of states, and the scattering states in real space.

II. COMPUTATIONAL METHODS

First-principles density-functional theory calculations are performed using the plane-wave pseudopotential method implemented in the QUANTUM ESPRESSO package [51]. Exchange and correlations are treated at the level of the generalized gradient approximation (GGA). An energy cutoff of 544 eV is used for the plane-wave expansion. Atomic relaxations are performed with a $6 \times 6 \times 1$ k-point mesh until the Hellmann-Feynman forces on each atom become less than 26 meV/Å. A $10 \times 10 \times 1$ k-point mesh is used in the subsequent self-consistent calculations.

We consider a FTJ made of $La_{0.5}Sr_{0.5}MnO_3$ electrodes and a $BaTiO_3$ tunnel barrier. First, we build a periodic supercell which consists of 8.5 unit cells (u.c.) of LSMO and 11.5 u.c. of BTO stacked along the [001] direction [Fig. 1(a)]. Following the experimental result of Ref. [47], we assume $La_{0.5}Sr_{0.5}O/TiO_2$ termination on both interfaces. The La-Sr substitutional doping is treated within the virtual crystal approximation (VCA), by modeling each A-site cation in LSMO with a pseudopotential of fractional valence [52]. The in-plane lattice constant a of the supercell is constrained to the calculated value of cubic $SrTiO_3$, $a = 3.931$ Å, to simulate epitaxial growth on a $SrTiO_3$ (001) substrate. The out-of-plane lattice constant as well as atomic coordinates are fully relaxed. The in-plane constraint produces tetragonal structure of bulk LSMO with $c/a = 0.977$ and bulk BTO with $c/a = 1.053$. The polarization P of BTO computed using the Berry phase method [53] is $P \approx 48\,\mu C/cm^2$, which is in line with the previous results [23,54].

Then, the electron transmission is calculated using a general scattering formalism implemented in QUANTUM ESPRESSO [55,56]. The supercell described above is used as the scattering region, ideally attached on both sides to semi-infinite LSMO leads. This structure represents a FTJ, which has open boundary conditions in the z direction but is periodic in the x-y plane. The latter property makes the Bloch wave vector $\mathbf{k}_\parallel = (k_x, k_y)$ a good quantum number, so that transmission T is a function of $\mathbf{k}_\parallel$. For calculating transmission, the two-dimensional Brillouin zone is sampled using a uniform $100 \times 100\,\mathbf{k}_\parallel$ mesh. In addition to the transmission, we consider the scattering states [55,56] in real space to analyze transport properties.

III. ATOMIC STRUCTURE

First, we examine the atomic structure of a LSMO/BTO/LSMO tunnel junction. We compare the two possible polarization states in the junction: a uniformly polarized state and a head-to-head domain-wall state.

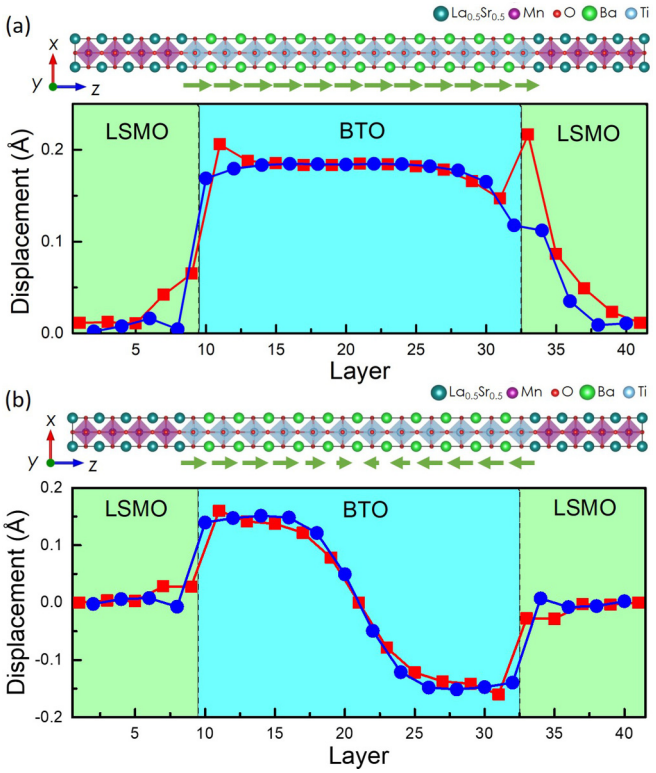

FIG. 1. (a) Relaxed atomic structure (top panel) and relative displacements between metal (M) and oxygen (O) atoms (bottom panel): $La_{0.5}Sr_{0.5}$-O, Ba-O (red squares), and Ti-O, Mn-O (blue circles) for a LSMO/BTO/LSMO tunnel junction in a uniformly polarized state. (b) Same as (a) in a head-to-head domain-wall state. In the BTO region, positive (negative) displacements correspond to polarization pointing to the right (left), as indicated by arrows in the top panels.

In order to simulate a uniformly polarized state, we displace the initial atomic positions of the metal atoms from their centrosymmetric positions along the z direction and then fully relax the atomic structure. Figure 1(a) shows the resulting displacements between metal and oxygen atoms across the FTJ. We see that the displacements are nearly uniform in the BTO layer giving rise to a uniform-polarization state as expected. The displacement magnitude of about 0.18 Å for the central BTO layers is nearly the same as that calculated for bulk BTO. It is notable that the $(La_{0.5}Sr_{0.5})$-O ionic displacement at the right interface is significantly enhanced. This stems from the electrostatic force between the positive polarization charge of BTO and the positive ionic charge of the interfacial $(La_{0.5}Sr_{0.5})$-O ionic layer consistent with the previous calculation [52].

In order to simulate a head-to-head domain-wall state, we set the initial displacements of the metal atoms from their centrosymmetric positions to be mirror images with respect to the middle of the BTO barrier. Normally, such a wall is energetically unfavorable due to the uncompensated polarization charge of $2P$ at the domain wall. However, the assumed $La_{0.5}Sr_{0.5}O/TiO_2$ interface termination is essentially

equivalent to electron doping of the structure, resulting in the partial screening of the polarization charge at the domain wall. This is evident from the nominal ionic charges across the FTJ. The LSMO consists of nominally charged $(La_{0.5}Sr_{0.5}O)^{0.5+}$ and $(MnO_2)^{0.5-}$ layers, whereas the BTO consists of neutral $(BaO)^0$ and $(TiO_2)^0$ layers. Thus, the $(La_{0.5}Sr_{0.5}O)^{0.5+}/(TiO_2)^0$ terminated interfaces are polar and have an effective interfacial bound charge of $\sigma_i \approx +0.25\, e/a^2$. The released negative charge of $-0.5\, e/a^2$ moves to the center the junction where it partially screens the positive polarization charge, thus supporting the formation of the ferroelectric head-to-head domain wall. The overall charge balance across the FTJ is summarized in Sec. IV.

The result of the atomic structure optimization of the FTJ is shown in Fig. 1(b). It is seen that the atomic displacements have opposite sign in the left (positive) and right (negative) regions of BTO. Close to the interfaces, the Ba-O and Ti-O displacements are uniform and are about 0.15 Å. This value is similar to that which we find for the ferroelectric strained bulk BTO. Closer to the middle of the barrier layer, the magnitude of these displacements varies rapidly, and the polarization changes sign in the middle of the barrier. This reveals the presence of a head-to-head domain wall in the BTO layer. Similar behavior has been predicted previously, where La doping in the middle of a $SrTiO_3$ barrier induced a tail-to-tail domain wall [57].

We note that the calculated total energy for the uniform-polarization state is predicted to be about 50 meV lower than for the head-to-head domain-wall state. Thus, in the considered LSMO/BTO/LSMO FTJ the domain-wall state is metastable. If such a state is destroyed by applying a sufficiently large electric field, it cannot be restored. This behavior is similar to what has been observed experimentally by Sanchez-Santolino *et al.* [47]. It would be interesting to find conditions where the domain-wall state represents a global minimum and the system could be reversibly switched between a uniform-polarization state and a head-to-head domain-wall state.

IV. ELECTRONIC STRUCTURE

Next, we calculate the electronic structure of the FTJ. Figure 2 shows the calculated layer-resolved local density of states (LDOS) projected onto the TiO monolayers. For the uniform-polarization state [Fig. 2(a)], the band edges, i.e., the conduction band minimum (CBM) and the valence band maximum (VBM), vary linearly across the BTO layer [orange lines in Fig. 2(a)]. This is due to the electric field resulting from the opposite-sign polarization charges at the two interfaces induced by uniform polarization of BTO. The electric field is screened in the LSMO electrodes. Thickness of the BTO layer is sufficiently large so that the Fermi energy crosses the CBM of BTO near the right interface (at about 3 u.c. from the interface).

For the ferroelectric polarization state forming the head-to-head domain-wall structure [Fig. 2(b)], we find a V-shaped electrostatic potential energy profile with a dip located at the domain wall. This is reflected in the variation of the CBM and VBM, across the BTO layer [orange lines in Fig. 2(b)]. The Fermi energy, E_F, is about 0.17 eV above the CBM for the middle TiO monolayers, whereas it lies below the CBM for

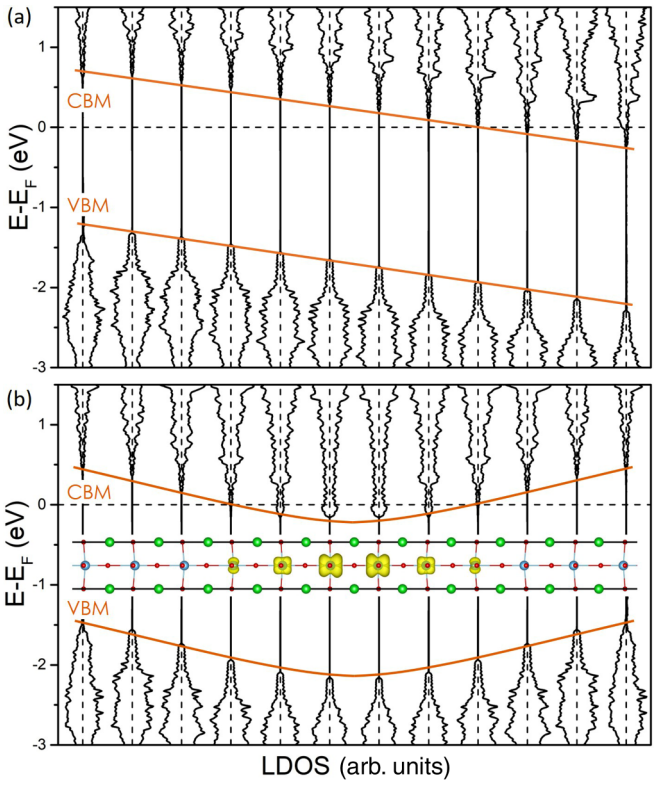

FIG. 2. Spin- and layer-resolved local density of states (LDOS) projected onto the TiO_2 monolayers in the BTO region for a uniform-polarization state (a) and a head-to-head domain-wall state (b). The majority-spin and minority-spin LDOS are plotted on the left and right, respectively. The orange lines indicate the variation in CBM and VBM across the BTO layer. The dashed line shows the Fermi energy. Inset in (b): Layer-resolved charge density, which is obtained by integrating the LDOS from the CBM to the Fermi energy.

the TiO monolayers adjacent to the interfaces. This implies electron accumulation in the middle of the BTO layer, i.e., the formation of a 2DEG at the ferroelectric domain wall. The real-space charge density of the 2DEG, obtained by integrating the LDOS from the CBM up to the Fermi energy, resides mostly on the Ti d_{xz} and d_{yz} orbitals and the charge density decreases monotonically away from the domain-wall center [see inset of Fig. 2(b)]. The 2DEG, which is created by the V-shaped electrostatic potential due to the ferroelectric domain wall, is responsible for resonant tunneling, as discussed below.

The resulting charge distribution in the FTJ, extracted from the calculated charge density, is consistent with the electrostatic picture discussed in Sec. II. The 2DEG charge density is $\sigma_{2DEG} \approx -0.69\ e/a^2$ [58]. This charge does not fully screen the polarization charge at the domain wall of $2P \approx +0.96\ e/a^2$, as is estimated from the calculated bulk value of BTO polarization. The net positive charge at the domain wall of $\sigma_{DW} \approx +0.27\ e/a^2$ produces an electric field $E = \sigma_{DW}/2\varepsilon$, pointing away from the domain wall (here ε is the background dielectric permittivity of BTO). The electric field in BTO (estimated from the potential slope in Fig. 2) is $E \approx 0.033\,\mathrm{V/Å}$ resulting in $\varepsilon \approx 48\varepsilon_0$. The polarization charge at the interfaces is $P \approx -0.48\ e/a^2$, which overrides a positive interface charge $\sigma_i \approx +0.25\ e/a^2$, resulting in the

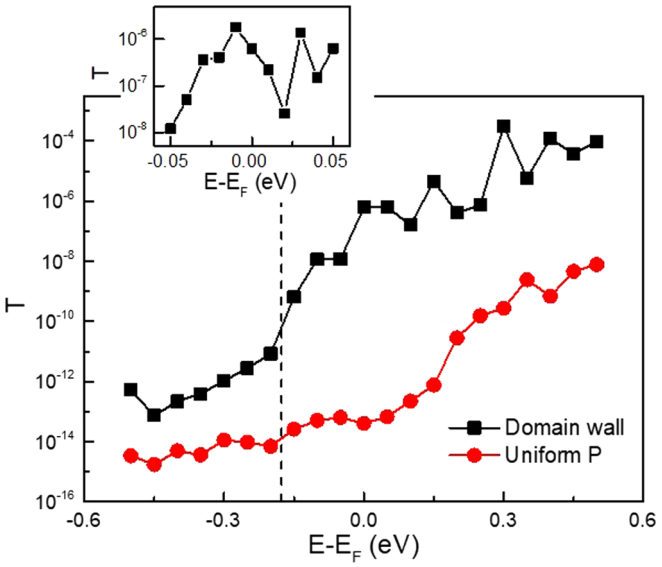

FIG. 3. Transmission T per unit cell area, a^2, across the LSMO/BTO/LSMO tunnel junction as a function of energy E, for the uniform-polarization state (red circles) and the head-to-head domain-wall state (black squares). The vertical dashed line denotes the CBM. The inset shows $T(E)$ on a finer scale around the Fermi energy for the domain-wall state.

net interface charge of $-0.23\,e/a^2$. To fully screen the electric field in LSMO, hole accumulation of $+0.095\,e/a^2$ is produced in LSMO at each interface.

We note that our model does not involve oxygen vacancies, which were put forward by Sanchez-Santolino *et al.* [47] to explain their experimental observations. The ferroelectric head-to-head domain wall can be stabilized as long as there are free electrons available to screen the polarization charge in the middle of the junction. The polar discontinuity at the interfaces serves as the source of the screening charge that stabilizes a head-to-head domain wall.

V. TRANSMISSION

Then, we explore the electron transport properties of the FTJ. Figure 3 shows the calculated electron transmission T of the junction as a function of electron energy E. For the uniformly polarized state (red symbols in Fig. 3), the transmission increases with increasing energy, reflecting a decrease in the potential barrier height when E is approaching the CBM, as well as a contribution from a reduced barrier width due to the band bending across the BTO barrier layer [Fig. 2(a)].

For the domain-wall state (black symbols in Fig. 3), the transmission across the FTJ is significantly higher than for the uniformly polarized state. For example, there is almost eight orders of magnitude enhancement of the transmission at the Fermi energy. Such a dramatic increase of transmission for the domain-wall state arises from resonant tunneling through the 2DEG created by the ferroelectric domain wall, as discussed below.

As seen from Fig. 2, for energies within the gap of the BTO barrier, $E - E_F < -0.2$ eV, the domain-wall state

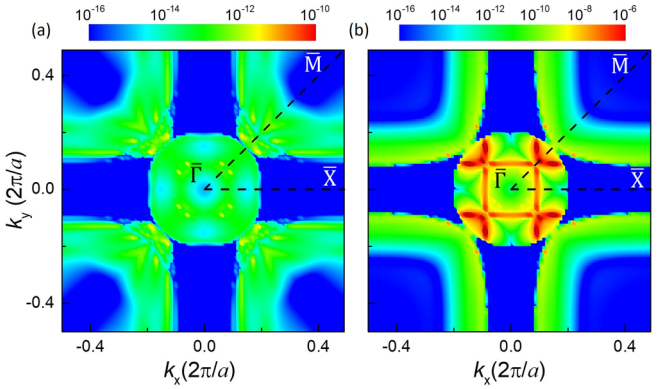

FIG. 4. $\mathbf{k}_\parallel$-resolved transmission across the LSMO/BTO/LSMO tunnel junction calculated at the Fermi energy for a uniformly polarized state (a) and a domain-wall state (b). High-symmetry points and lines are indicated in the two-dimensional Brillouin zone.

transmission is relatively low. For these energies, the transmission is controlled by direct tunneling across the BTO barrier and increases with energy as the result of the reducing barrier height. Note that the domain-wall state transmission is larger than the uniformly polarized state transmission even at these energies due to a lower barrier height for the former.

There is a sharp increase in the transmission at $E - E_F \approx -0.17$ eV (as indicated by the vertical dashed line in Fig. 3), corresponding to the CBM in the central region of BTO [Fig. 2(b)]. This jump is a result of resonant tunneling through localized electronic states in the barrier layer associated with the 2DEG at the ferroelectric domain wall. The resonant contributions are evident by the appearance of alternative features in the T versus E plot, where the peaks and deeps in T appear in irregular fashion (inset in Fig. 3). A further increase in energy leads to a nonmonotonic increase in transmission. The upward trend is due to the fact that there are in general more quantum-well states which contribute to resonant tunneling at higher energy. However, the number of such states is not proportional to the energy.

To analyze the resonant tunneling mechanism, we calculate the transmission probability as a function of the transverse wave vector $\mathbf{k}_\parallel$ (which is conserved in the process of tunneling) in the two-dimensional Brillouin zone (2DBZ) at the Fermi energy. Figure 4(a) shows the result of this calculation for the uniformly polarized state. It is seen that there is a circular region around the $\bar{\Gamma}$ point ($\mathbf{k}_\parallel = 0$) and four arcs around the 2DBZ corners where the transmission is sizable. This shape of the transmission contour reflects the Fermi surface of LSMO projected onto the (001) plane perpendicular to the transport direction, i.e., the region in the 2DBZ where the propagating Bloch states are available in the electrodes, and consistent with the previous calculations [23,52].

Figure 4(b) shows the $\mathbf{k}_\parallel$-resolved transmission for the domain-wall state of the FTJ. It is seen that in addition to the transmission contours similar to those for the uniformly polarized state [colored in green and blue in Figs. 4(a) and 4(b)], there are a number of hot spots, i.e., areas of high transmission colored in red in Fig. 4(b). These hot spots dominate the total transmission, despite their relatively small area in the 2DBZ,

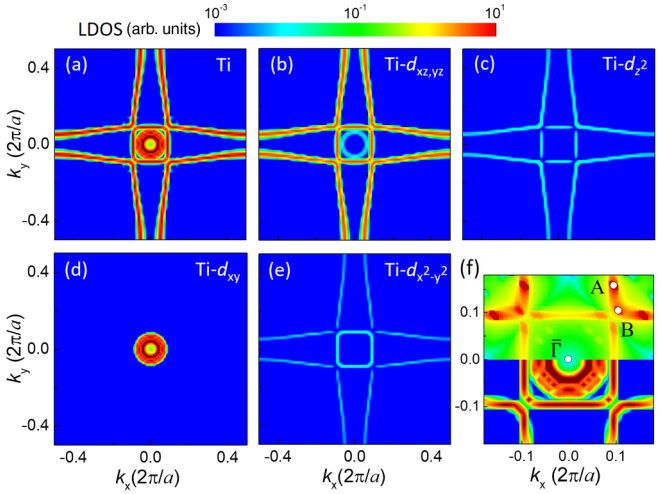

FIG. 5. $\mathbf{k}_\parallel$- and orbital-resolved local density of states (LDOS) at the Fermi energy: total LDOS (a) and orbital-resolved LDOS at the central Ti atom: $d_{xz,yz}$ (b), d_{z^2} (c), d_{xy} (d), and $d_{x^2-y^2}$ (e) orbitals. (f) Combined $\mathbf{k}_\parallel$-resolved LDOS [bottom panel, same as in (a)] and transmission [top panel, same as in Fig. 4(b)] in the central part of the 2DBZ. A and B denote the $\mathbf{k}_\parallel$ points at which the scattering states are calculated and shown in Figs. 6(b) and 6(c), respectively.

and originate from resonant tunneling through the localized electron states formed at the head-to-head ferroelectric domain wall.

In order to understand the origin and placement of the hot spots, we plot in Fig. 5(a) the $\mathbf{k}_\parallel$-resolved LDOS projected onto the central Ti atom at the Fermi energy. The LDOS reveals narrow regions of high density associated with the electronic states forming the 2DEG. To correlate the $\mathbf{k}_\parallel$-resolved LDOS and transmission, we display in two panels of Fig. 5(f) the LDOS (bottom) and the transmission (top) in the central part of the 2DBZ. It is evident that there is a clear match between the two, in the form and position of a square-shaped feature and four arcs around the $\bar{\Gamma}$ point. It is also notable that the states located in a circular region with high LDOS lying closer to the $\bar{\Gamma}$ point do not contribute much to transmission.

To understand this behavior, we project the LDOS for the central Ti atom onto the $3d$ orbitals, as shown in Figs. 5(b)–5(e). We find that there is a large LDOS in the hot-spot transmission regions contributed by the Ti-$d_{xz,yz}$ orbitals [Fig. 5(c)], which are also seen in the charge density shown in the inset of Fig. 2. States of this symmetry are, however, absent in the LSMO electrodes, where the central part of the Fermi surface in the 2DBZ is composed of the states predominantly of the d_{z^2} character [52,59]. We therefore argue that the Ti-$d_{xz,yz}$ states localized at the BTO domain wall participate in the transmission due to their hybridization with the Ti-d_{z^2} orbitals. Indeed, as the symmetry is lowered from D_4 at the $\bar{\Gamma}$ point to C_2 at point B in Fig. 5(f), the Ti-$d_{xz,yz}$ doublet splits and it becomes compatible in symmetry with the Ti-d_{z^2} state symmetry enabling hybridization away from the zone center. This is evident from the shape of the Ti-d_{z^2} projected LDOS in the central part of the 2DBZ [Fig. 5(d)] being nearly identical to that seen in the hot-spot transmission distribution [Fig. 4(a)]. The circular feature in the $\mathbf{k}_\parallel$-resolved LDOS around the $\bar{\Gamma}$ point is due the Ti-d_{xy} orbitals [Fig. 5(e)]. These orbitals are localized in the xy plane perpendicular to the transport direction and do not contribute to the conductance.

Finally, we exclude a possible contribution from resonant tunneling associated with the interface states. It is known that, for a symmetric tunnel junction, resonant transmission may occur due to two localized interface states matched in energy [60,61]. However, in our case, the transmission hot spots do not match the interface states, as we find from comparison of the $\mathbf{k}_\parallel$-resolved LDOS projected onto the interfacial Mn atom (not shown) and the $\mathbf{k}_\parallel$-resolved transmission.

The resonant nature of tunneling is clearly seen from the amplitude of the electron transmission function. In Fig. 6 we plot scattering states in real space (a squared wave function of

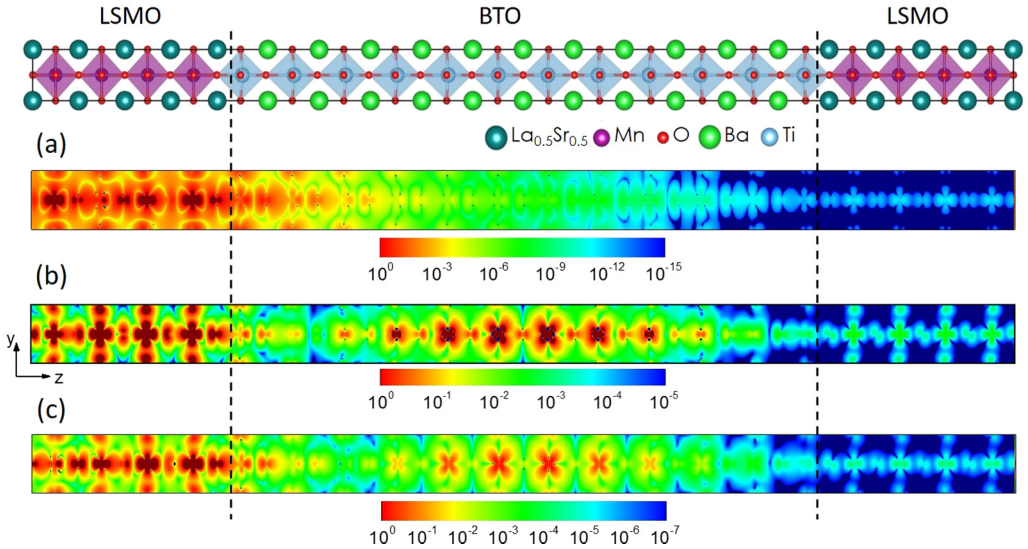

FIG. 6. (a) Real-space scattering states across the LSMO/BTO/LSMO tunnel junction calculated at the Fermi energy for different $\mathbf{k}_\parallel$ points: $\mathbf{k}_\parallel = (0,0)$ (a), $\mathbf{k}_\parallel = (0.09,0.15)$ (b), and $\mathbf{k}_\parallel = (0.1,0.1)$ (c), where the values of $\mathbf{k}_\parallel$ are given in units of $2\pi/a$. The two latter $\mathbf{k}_\parallel$ points are indicated in Fig. 5(f) as points A and B, respectively.

the right-moving state) across the LSMO/BTO/LSMO tunnel junction at several selected $\mathbf{k}_\parallel$ points. At the $\bar{\Gamma}$ point, the electron state incident from the left LSMO electrode decays exponentially when traveling through the BTO barrier layer [Fig. 6(a)], indicating the direct tunneling mechanism for electron transmission. We find that the scattering state is composed of Mn (Ti)-d_{z^2} orbitals and O-p_z orbitals. These orbitals constitute the Δ_1-symmetry band, which dominates the transmission across the FTJ. In contrast, for $\mathbf{k}_\parallel$ corresponding to the transmission hot spots, the behavior is quite different. The amplitudes of the scattering states corresponding to the $\mathbf{k}_\parallel$ points A and B in Fig. 5(f) are plotted in Figs. 6(b) and 6(c), respectively. The amplitude is dramatically enhanced around the central region of the BTO barrier layer where the 2DEG is present. Such behavior is typical for resonant tunneling, where the evanescent state creates a node at a localized state. The shape of the scattering wave amplitude around the domain wall indicates that the scattering state in this region is composed of the Ti-d_{yz} and Ti-d_{xz} orbitals, which is consistent with the previous discussion.

VI. CONCLUSIONS

In summary, using first-principles density-functional theory calculations, we have explored electronic and transport properties of a LSMO/BTO/LSMO ferroelectric tunnel junction with a head-to-head ferroelectric domain wall embedded in the BTO barrier layer. We demonstrated that such a charged domain wall can be stabilized by the presence of negative charge in the barrier arising from the polar $(La_{0.5}Sr_{0.5}O)^{0.5+}/(TiO_2)^0$ terminated interfaces. The resulting V-shaped electrostatic potential profile across the BTO layer creates a quantum well supporting a 2DEG. Our transport calculations show that the confined electronic states in the tunneling barrier lead to resonant transmission across the FTJ. The resonant tunneling occurs in the specific $\mathbf{k}_\parallel$ points of the two-dimensional Brillouin zone, when the incoming electron energy matches a quantum-well state. These conductance hot spots are responsible for the experimentally observed resonant spikes in the differential conductance as a function voltage [47]. We also find that this resonant tunneling is highly selective of the orbital symmetry of the tunneling states due to the orbital polarization of the 2DEG. The resonant tunneling mechanism enhances the conductance of the FTJ by many orders of magnitude as compared to the single domain state. This phenomenon serves as the foundation of an alternative type of electroresistance effect if the energy of the domain-wall state could be lowered below that of the single-domain state and the device can be switched between the two states by an electric field. We hope that our results will further stimulate experimental efforts in the understanding of the electron transport across ferroelectric domain walls and provide some guidelines for designing multifunctional electronic devices.

ACKNOWLEDGMENTS

This work was supported by the National Science Foundation (NSF) through Nebraska Materials Research Science and Engineering Center (MRSEC) (NSF Grant No. DMR-1420645). Computations were performed at the University of Nebraska Holland Computing Center. Some of the figures were produced using VESTA software [62].

[1] *Physics of Ferroelectrics: A Modern Perspective*, edited by K. M. Rabe, C. H. Ahn, and J.-M. Triscone (Springer, New York, 2007).
[2] D. D. Fong, G. B. Stephenson, S. K. Streiffer, J. A. Eastman, O. Auciello, P. H. Fuoss, and C. Thompson, Science **304**, 1650 (2004).
[3] C. Lichtensteiger, J.-M.Triscone, J. Junquera, and P. Ghosez, Phys. Rev. Lett. **94**, 047603 (2005).
[4] D. A. Tenne, A. Bruchhausen, N. D. Lanzillotti-Kimura, A. Fainstein, R. S. Katiyar, A. Cantarero, A. Soukiassian, V. Vaithyanathan, J. H. Haeni, W. Tian, D. G. Schlom, K. J. Choi, D. M. Kim, C. B. Eom, H. P. Sun, X. Q. Pan, Y. L. Li, L. Q. Chen, Q. X. Jia, S. M. Nakhmanson *et al.*, Science **313**, 1614 (2006).
[5] J. F. Scott, Science **315**, 954 (2007).
[6] E. Y. Tsymbal and H. Kohlstedt, Science **313**, 181 (2006).
[7] V. Garcia and M. Bibes, Nat. Commun. **5**, 4289 (2014).
[8] J. P. Velev, J. D. Burton, M. Y. Zhuravlev, and E. Y. Tsymbal, npj Comput. Mater. **2**, 16009 (2016).
[9] M. Y. Zhuravlev, R. F. Sabirianov, S. S. Jaswal, and E. Y. Tsymbal, Phys. Rev. Lett. **94**, 246802 (2005).
[10] H. Kohlstedt, N. A. Pertsev, J. Rodríguez Contreras, and R. Waser, Phys. Rev. B **72**, 125341 (2005).
[11] A. Chanthbouala, A. Crassous, V. Garcia, K. Bouzehouane, S. Fusil, X. Moya, J. Allibe, B. Dlubak, J. Grollier, S. Xavier, C. Deranlot, A. Moshar, R. Proksch, N. D. Mathur, M. Bibes, and A. Barthelemy, Nat. Nanotechnol. **7**, 101 (2012).
[12] D. J. Kim, H. Lu, S. Ryu, C.-W. Bark, C.-B. Eom, E. Y. Tsymbal, and A. Gruverman, Nano Lett. **12**, 5697 (2012).
[13] Z. Wen, C. Li, D. Wu, A. Li, and N. B. Ming, Nat. Mater. **12**, 617 (2013).
[14] H. Lu, A. Lipatov, S. Ryu, D. J. Kim, H. Lee, M. Y. Zhuravlev, C. B. Eom, E. Y. Tsymbal, A. Sinitskii, and A. Gruverman, Nat. Commun. **5**, 5518 (2014).
[15] S. Boyn, A. M. Douglas, C. Blouzon, P. Turner, A. Barthelemy, M. Bibes, S. Fusil, J. M. Gregg, and V. Garcia, Appl. Phys. Lett. **109**, 232902 (2016).
[16] Z. Xi, J. Ruan, C. Li, C. Zheng, Z. Wen, J. Dai, A. Li, and D. Wu, Nat. Commun. **8**, 15217 (2017).
[17] S. Boyn, S. Girod, V. Garcia, S. Fusil, S. Xavier, C. Deranlot, H. Yamada, C. Carrétéro, E. Jacquet, M. Bibes, A. Barthélémy, and J. Grollier, Appl. Phys. Lett. **104**, 052909 (2014).
[18] M. Abuwasib, H. Lu, T. Li, P. Buragohain, H. Lee, C.-B. Eom, A. Gruverman, and U. Singisetti, Appl. Phys. Lett. **108**, 152904 (2016).
[19] A. Zenkevich, M. Minnekaev, Yu. Matveyev, Yu. Lebedinskii, K. Bulakh, A. Chouprik, A. Baturin, K. Maksimova, S. Thiess, and W. Drube, Appl. Phys. Lett. **102**, 062907 (2013).
[20] X. Liu, J. D. Burton, and E. Y. Tsymbal, Phys. Rev. Lett. **116**, 197602 (2016).

[21] R. Soni, A. Petraru, P. Meuffels, O. Vavra, M. Ziegler, S. K. Kim, D. S. Jeong, N. A. Pertsev, and H. Kohlstedt, Nat. Commun. **5**, 5414 (2014).

[22] L. L. Tao and J. Wang, J. Appl. Phys. **119**, 224104 (2016).

[23] J. D. Burton and E. Y. Tsymbal, Phys. Rev. Lett. **106**, 157203 (2011).

[24] A. Tsurumaki-Fukuchi, H. Yamada, and A. Sawa, Appl. Phys. Lett. **103**, 152903 (2013).

[25] V. S. Borisov, S. Ostanin, S. Achilles, J. Henk, and I. Mertig, Phys. Rev. B **92**, 075137 (2015).

[26] L. L. Tao and J. Wang, Appl. Phys. Lett. **108**, 062903 (2016).

[27] D. I. Bilc, F. D. Novaes, J. Íñiguez, P. Ordejón, and P. Ghosez, ACS Nano **6**, 1473 (2012).

[28] A. Useinov, A. Kalitsov, J. Velev, and N. Kioussis, Appl. Phys. Lett. **105**, 102403 (2014).

[29] M. Y. Zhuravlev, S. S. Jaswal, E. Y. Tsymbal, and R. F. Sabirianov, Appl. Phys. Lett. **87**, 222114 (2005).

[30] J. P. Velev, C. G. Duan, J. D. Burton, A. Smogunov, M. K Niranjan, E. Tosatti, S. S. Jaswal, and E. Y. Tsymbal, Nano Lett. **9**, 427 (2009).

[31] M. Y. Zhuravlev, S. Maekawa, and E. Y. Tsymbal, Phys. Rev. B **81**, 104419 (2010).

[32] V. Garcia, M. Bibes, L. Bocher, S. Valencia, F. Kronast, A. Crassous, X. Moya, S. Enouz-Vedrenne, A. Gloter, D. Imhoff, C. Deranlot, N. D. Mathur, S. Fusil, K. Bouzehouane, and A. Barthelemy, Science **327**, 1106 (2010).

[33] D. Pantel, S. Goetze, D. Hesse, and M. Alexe, Nat. Mater. **11**, 289 (2012).

[34] Y. W. Yin, J. D. Burton, Y.-M. Kim, A. Y. Borisevich, S. J. Pennycook, S. M. Yang, T. W. Noh, A. Gruverman, X. G. Li, E. Y. Tsymbal, and Q. Li, Nat. Mater. **12**, 397 (2013).

[35] G. Catalan, J. Seidel, R. Ramesh, and J. F. Scott, Rev. Mod. Phys. **84**, 119 (2012).

[36] X. Wu and D. Vanderbilt, Phys. Rev. B **73**, 020103(R) (2006).

[37] J. Seidel, L. W. Martin, Q. He, Q. Zhan, Y.-H. Chu, A. Rother, M. E. Hawkridge, P. Maksymovych, P. Yu, M. Gajek, N. Balke, S. V. Kalinin, S. Gemming, F. Wang, G. Catalan, J. F. Scott, N. A. Spaldin, J. Orenstein, and R. Ramesh, Nat. Mater. **8**, 229 (2009).

[38] S. Farokhipoor and B. Noheda, Phys. Rev. Lett. **107**, 127601 (2011).

[39] J. Guyonnet, I. Gaponenko, S. Gariglio, and P. Paruch, Adv. Mater. **23**, 5377 (2011).

[40] D. Meier, J. Seidel, A. Cano, K. Delaney, Y. Kumagai, M. Mostovoy, N. A. Spaldin, R. Ramesh, and M. Fiebig, Nat. Mater. **11**, 284 (2012).

[41] W. Wu, Y. Horibe, N. Lee, S.-W. Cheong, and J. R. Guest, Phys. Rev. Lett. **108**, 077203 (2012).

[42] P. Maksymovych, A. N. Morozovska, P. Yu, E. A. Eliseev, Y.-H. Chu, R. Ramesh, A. P. Baddorf, and S. V. Kalinin, Nano Lett. **12**, 209 (2012).

[43] M. Schröder, A. Haußmann, A. Thiessen, E. Soergel, T. Woike, and L. M. Eng, Adv. Funct. Mater. **22**, 3936 (2012).

[44] T. Sluka, A. K. Tagantsev, P. Bednyakov, and N. Setter, Nat. Commun. **4**, 1808 (2013).

[45] R. K. Vasudevan, M. B. Okatan, C. Duan, Y. Ehara, H. Funakubo, A. Kumar, S. Jesse, L.-Q. Chen, S. V. Kalinin, and V. Nagarajan, Adv. Funct. Mater. **23**, 2592 (2013).

[46] I. Stolichnov, L. Feigl, L. J. McGilly, T. Sluka, X. K. Wei, E. Colla, A. Crassous, K. Shapovalov, P. Yudin, A. K. Tagantsev, and N. Setter, Nano Lett. **15**, 8049 (2015).

[47] G. Sanchez-Santolino, J. Tornos, D. Hernandez-Martin, J. I. Beltran, C. Munuera, M. Cabero, A. Perez-Muñoz, J. Ricote, F. Mompean, M. Garcia-Hernandez, Z. Sefrioui, C. Leon, S. J. Pennycook, M. C. Muñoz, M. Varela, and J. Santamaria, Nat. Nanotechnol. **12**, 655 (2017).

[48] K. Rahmanizadeh, D. Wortmann, G. Bihlmayer, and S. Blügel, Phys. Rev. B **90**, 115104 (2014).

[49] J. Q. Dai, H. Zhang, and Y. M. Song, J. Appl. Phys. **114**, 163703 (2013).

[50] E. Y. Tsymbal and J. P. Velev, Nat. Nanotechnol. **12**, 614 (2017).

[51] P. Giannozzi, S. Baroni, N. Bonini, M. Calandra, R. Car, C. Cavazzoni, D. Ceresoli, G. L. Chiarotti, M. Cococcioni, I. Dabo *et al.*, J. Phys.: Condens. Matter **21**, 395502 (2009).

[52] J. D. Burton and E. Y. Tsymbal, Phys. Rev. B **93**, 024419 (2016).

[53] R. D. King-Smith and D. Vanderbilt, Phys. Rev. B **47**, 1651 (1993).

[54] J. D. Burton and E. Y. Tsymbal, Phys. Rev. B **80**, 174406 (2009).

[55] H. J. Choi and J. Ihm, Phys. Rev. B **59**, 2267 (1999).

[56] A. Smogunov, A. Dal Corso, and E. Tosatti, Phys. Rev. B **70**, 045417 (2004).

[57] J. D. Burton, J. P. Velev, and E. Y. Tsymbal, Phys. Rev. B **80**, 115408 (2009).

[58] The 2DEG charge density is obtained by integrating the total minority-spin charge density from the CBM up to the Fermi energy and then multiplying by two. Since the LSMO is half-metallic and there are no minority-spin bands in this energy window in the electrodes, all the integrated charge density comes entirely from 2DEG being equally distributed between the majority- and minority-spin states.

[59] L. L. Lev, J. Krempaský, U. Staub, V. A. Rogalev, T. Schmitt, M. Shi, P. Blaha, A. S. Mishchenko, A. A. Veligzhanin, Y. V. Zubavichus, M. B. Tsetlin, H. Volfová, J. Braun, J. Minár, and V. N. Strocov, Phys. Rev. Lett. **114**, 237601 (2015).

[60] O. Wunnicke, N. Papanikolaou, R. Zeller, P. H. Dederichs, V. Drchal, and J. Kudrnovský, Phys. Rev. B **65**, 064425 (2002).

[61] K. D. Belashchenko, J. Velev, and E. Y. Tsymbal, Phys. Rev. B **72**, 140404(R) (2005).

[62] K. Momma and F. Izumi, J. Appl. Crystallogr. **44**, 1272 (2011).